Journal of Materials Chemistry A

ROYAL SOCIETY OF CHEMISTRY

PAPER

View Article Online
View Journal | View Issue

Check for updates

Cite this: J. Mater. Chem. A, 2025, 13, 14773

Sustainable high-pressure homogenization of hexagonal boron nitride for triboelectric nanogenerators: advancing self-powered environmental monitoring in portable electronics†

Yawar Abbas, ‡[ab] Rohan B. Ambade, ‡[cd] Muhammad Umair Khan, [ae] Rui Chang,[cd] Yahya Zweiri,[cd] Baker Mohammad,[ae] Dalaver Anjum *[f] and Yarjan Abdul Samad *[cg]

The growing demand for low-power, high-density wearable electronics devices and Internet of Things (IoT) technology requires reliable energy modules. Triboelectric nanogenerators (TENGs), an emerging energy harvesting technology, hold great potential to consistently supply power to these IoT devices and low-power consumption devices. Herein, we demonstrate the fabrication of a highly efficient triboelectric nanogenerator (TENG) by synthesizing highly pure two-dimensional (2D) hexagonal boron nitride (hBN) flakes as electropositive materials using the high-pressure homogenizer (HPH) method and fluorinated ethylene propylene (FEP) as electronegative materials. The fabricated device exhibits a highly reliable and repeatable open circuit voltage (V_{oc}) of ~135 V and short circuit current (I_{sc}) of ~17.0 μA at a tapping frequency of 5 Hz. Furthermore, the 2D hBN flakes prepared by HPH exhibit a high-power density of 18 W cm^{-2}, exceeding the previously reported values for hBN-based TENGs. The device can monitor full-range humidity (30% to 100% RH) and distinguish between light and strong tapping. The HPH-prepared 2D hBN-based TENGs powered or operated portable devices such as digital thermometers, stopwatches, and mini-calculators. The HPH-prepared 2D hBN-based TENG device can harvest energy from the mechanical input for an energy-efficient lifestyle because it can continuously charge and discharge the capacitor through continuous pressing and releasing by tapping. Thus, HPH-prepared 2D hBN flakes can be used to create an energy-efficient process to convert mechanical energy into electrical energy, promote sustainability, and advance clean energy technologies.

Received 6th December 2024
Accepted 31st March 2025

DOI: 10.1039/d4ta08698h

rsc.li/materials-a

Introduction

Energy is abundant in our environment through electromagnetic waves, sound energy, mechanical energy, and so on, which can be converted into valuable electrical energy using appropriate transducers.[1] Energy harvesting techniques provide a viable solution for developing self-powered microsystems, as this technology eliminates the need for frequent battery replacements, which can pose a significant challenge in maintenance and sustainability.[1,2] Harnessing ambient stray energy through various technologies, such as photovoltaic, thermoelectric, piezoelectric, and triboelectric, can create a cleaner and more sustainable future.[1] In the quest for clean energy, various techniques have been used to convert mechanical energy into electrical energy, including piezoelectric, triboelectric, electromagnetic, electrostatic, and pyroelectric nanogenerators.[1–3] The triboelectric nanogenerators (TENGs) are transducers that have received immense interest due to their demonstrated high energy conversion efficiency and power density compared to other technologies.[1–3] TENGs generate high voltage through the triboelectrification effect and electrostatic induction.[4,5] In principle, TENGs are classified into four types based on their operating mechanisms, namely, contact-separation (CS) mode,[6,7] relative sliding (RS) mode,[8,9] free-standing (FS) mode,[10,11] and single electrode mode.[12,13] The fundamental

[a]Center for Cyber-Physical Systems - System on Chip Lab, Khalifa University of Science & Technology, 127788, Abu Dhabi, United Arab Emirates
[b]James Watt School of Engineering, University of Glasgow, Glasgow, G12 8QQ, UK
[c]Department of Aerospace Engineering, Khalifa University of Science & Technology, 127788, Abu Dhabi, United Arab Emirates. E-mail: yarjan.abdulsamad@ku.ac.ae
[d]Advanced Research and Innovation Center, Khalifa University of Science & Technology, 127788, Abu Dhabi, United Arab Emirates
[e]Department of Computer and Information Engineering, Khalifa University, Abu Dhabi 127788, United Arab Emirates
[f]Department of Physics, Khalifa University of Science and Technology (KUST), P.O. Box 127788, Abu Dhabi, United Arab Emirates
[g]Cambridge Graphene Center, University of Cambridge, 9 JJ Thomson Avenue, Cambridge CB3 0FA, UK. E-mail: yy418@cam.ac.uk

† Electronic supplementary information (ESI) available. See DOI: https://doi.org/10.1039/d4ta08698h

‡ Contributed equally to this work.

energy harvesting mechanism in all these modes depends on combining the triboelectrification effect and electrostatic induction. The CS mode offers significant advantages over the other energy harvesting modes. These include better power generation, efficient ambient energy capture, easy fabrication, and reduced wear and tear of electropositive and electronegative layers.[14–16] A wide range of materials have been developed to generate voltage using TENGs.[17–19]

Two-dimensional (2D) materials have gained widespread attention due to their unique properties, such as remarkable physicochemical properties, excellent electronic and mechanical properties, high surface area, and excellent optical properties for their potential applications, including optoelectronics, energy storage, nanogenerators, electromagnetic shielding, and sensors.[20–25] The 2D materials encompass a wide range of compounds, including but not limited to graphene, graphene oxide (GO), MXenes, black phosphorus (BP), metal–organic frameworks (MOFs), transition metal dichalcogenides (TMDs), covalent–organic frameworks (COFs), and hexagonal boron nitride (hBN).[20–26] The manipulation of the chemistry and structure of 2D materials has emerged as a viable strategy for controlling their properties and producing high-performance devices. Such an approach offers the potential for facile tuning of electronic, optical, and mechanical properties, among others. Thus, the ability to control the properties of 2D materials through chemistry and structure manipulation represents a promising avenue for developing next-generation technologies.[26] 2D boron nitride (BN) flakes made from hBN have gained significant attention due to their exceptional properties owing to their ultrahigh thermal conductivity (751 W m^{-1} K^{-1}), structural stability, high-temperature stability with a decomposition temperature of 1272 K in air and 1673 K in vacuum, and impressive mechanical properties with a fracture strength of 68–215 GPa and a Young's modulus of 0.865 TPa.[27,28] The 2D hBN flakes can be produced by exfoliating bulk hBN.[10,11] This process unlocks the numerous advantages of 2D hBN material, which possesses a unique combination of properties, making it ideal for various applications in energy, electronics, and materials science.[29,30] Efforts to synthesize 2D hBN flakes in a highly efficient and scalable manner have received significant attention. Enhancing the synthesis methods on a large scale is a critical priority, and notable progress has been made. It is important to continue developing these techniques to meet the increasing demand for efficient and cost-effective processes. Different methods for obtaining 2D hBN flakes include ball milling, chemical exfoliation, wet chemical reactions, chemical vapor deposition (CVD), and electron irradiation.[29,30] Ball milling and chemical exfoliation *via* sonication are the most common exfoliation methods.[30] The liquid-phase exfoliation approach is simple to apply to obtain high-quality 2D hBN flakes. However, its yield is often low, and the lateral size is difficult to control because it relies on hBN bulk properties.[30] Although the yield is relatively high in the ball milling process (over 80%), it requires chemical additives (*e.g.*, urea, sugar, or sodium hydroxide), leading to 2D hBN functionalization. High-energy impacts result in smaller lateral sizes and defects (*e.g.*, vacancies, Stone–Wales, and line defects). Although it is widely used, mechanical exfoliation-based grinding technique has a significant disadvantage. It produces 2D hBN flakes smaller than 1 μm, limiting its effectiveness. Among the various techniques for preparing 2D hBN flakes, high-pressure homogenization (HPH) is a highly promising mechano-chemical method for synthesizing 2D materials that generate a solid force to reduce particle size and modify them into liquid samples.[31] HPH synthesis techniques deliver unparalleled scalability and exceptional efficiency in exfoliation processes using a combination of cavitation and shear forces.[31,32] This force can overcome the van der Waals forces between molecules, facilitating the delamination of layered materials.

In this work, we synthesized 2D hBN flakes with diameters of several nm using a highly promising mechano-chemical HPH method and utilized pure hBN flakes as an electropositive layer of TENG. The mechanically stable hBN flakes significantly enhanced the output performance of the fabricated TENG. The open circuit voltage (V_{oc}) of ~135 V for a load resistance of 20 MΩ demonstrates the efficient charge transfer ability of the TENG. In addition, the prepared TENG demonstrated continuous voltage generation of 20 000 cycles and self-powered humidity and pressure-sensitive characteristics. These results are due to the synergistic effect of defect-free and high mechanical strain on the HPH-prepared 2D hBN flakes, as revealed in the atomic scale high-resolution electron microscopy. The highly sensitive open circuit voltage and short circuit current of the prepared TENG demonstrate the robust characteristics of the device for powering low-powered portable devices and self-powered pressure and humidity sensors.

Results and discussion

Preparation of high-quality 2D hBN flakes *via* high-pressure homogenization process

The schematic shows the exfoliation process and the internal structure of the HPH equipment. This section presents the meticulously designed mechanisms of the HPH equipment for producing 2D hBN flakes (Scheme 1). During the HPH process, the bulk material undergoes intense forces such as high-velocity impact, sudden pressure drops, rapid shear, vibrations, and cavitation.[32–34] The high-pressure intensifier pump disperses raw materials into an interaction chamber, causing the liquid to flow through a narrow aperture at a rapid speed.[33] The HPH technique offers advantages over other processes for efficiently producing 2D nanosheets/flakes.[32–35] It combines shearing, crushing, and cavitation mechanisms, enabling the mass production of various 2D materials as a continuous and industrial-compatible process.[35] The HPH technique is highly valued for its consistency and reproducibility, particularly when exfoliating 2D materials, making it essential for research and industrial applications. During the HPH process of the hBN, the high-speed shear forces applied on the edge of the hBN effectively overcome the interaction between the boron nitride lamellae, generating exfoliated boron nitride. Shear flow affects the exfoliated boron nitride, causing stress concentration.[32–36] Excessive pressure or prolonged treatment can fracture the expanded boron nitride, resulting in smaller 2D hBN flakes.[33]

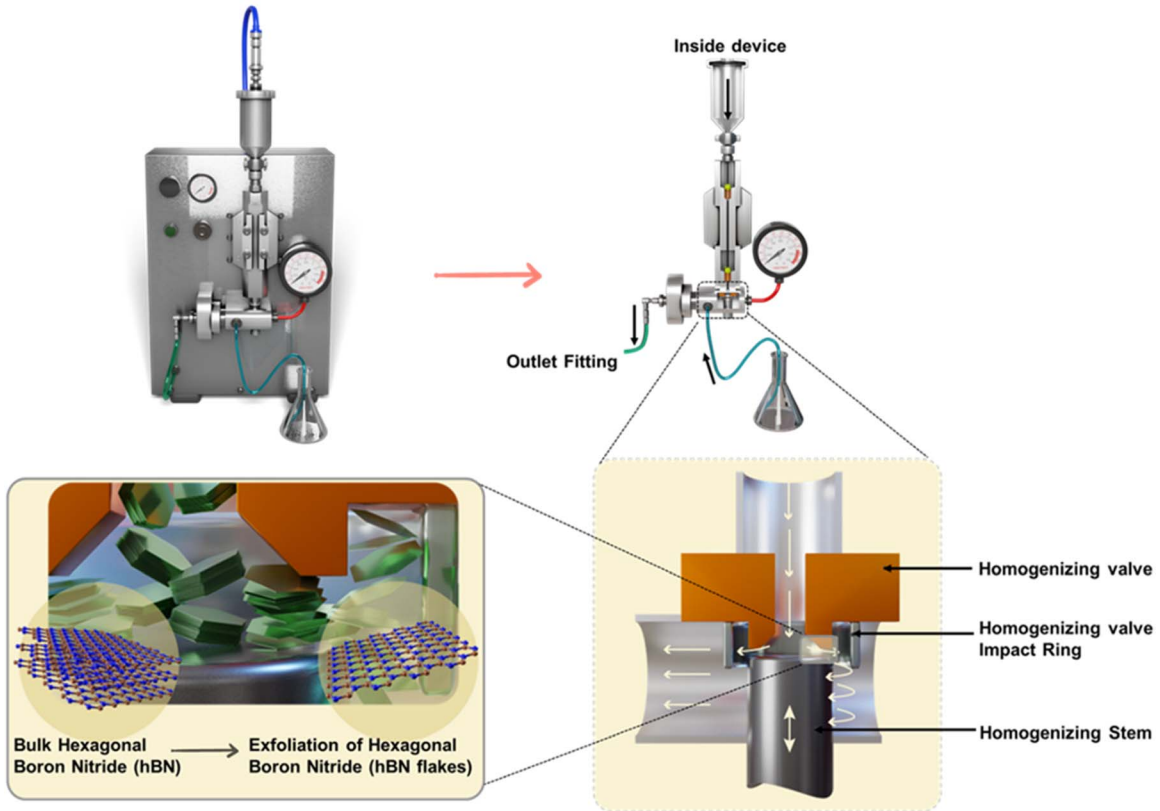

Scheme 1 Schematic illustration of the HPH process for preparing scalable 2D hBN flakes.

The AVESTIN "EmulsiFlex™-C3" was used in this work for the HPH process, featuring a double-walled stirred tank connected to a thermostat for feed suspension holdup and cooling. The EmulsiFlex™-C3 homogenizer features a high-pressure pump capable of achieving pressures up to 30 000 psi (2070 bar) for sample processing. Pre-homogenization was performed using a blade stirrer (1000 rpm) inside the tank with the suspension. The pressure was adjusted by changing the flow rate through a diameter nozzle (240 mm). The process starts by thoroughly mixing the bulk boron nitride and deionized water (DIW) and adding sodium deoxycholate (SDC). The resulting mixture undergoes the HPH process (as illustrated in Scheme 1), utilizing varying process cycles (1–100) at a maximum pressure of approximately 100 MPa for 10 min at room temperature to give a stable dispersion of hBN flakes in the DIW. The bulk hBN sample was introduced into the interaction chamber to induce high shear forces and turbulence *via* a small orifice under increased pressure. The bulk hBN passing through a small orifice at high velocity experiences extreme shear forces, leading to cavitation, which aids in the exfoliation of particles and the formation of a suspension.[33] The interaction chamber efficiently reduced the particle and droplet sizes, ensuring thorough homogenization of the 2D hBN flakes. The homogenization process was optimized by adjusting parameters such as the pressure, flow rate, and number of passes for hBN. The direct exfoliation of bulk hBN powder through HPH resulted in the dispersion of milky 2D hBN flakes.[32] The processed hBN material is cooled and subsequently collected from the outlet reservoir. The sample is subjected to multiple cycles within the system to enhance its homogenization efficiency. The dispersion of exfoliated 2D hBN flakes remained stable under ambient conditions.

The crystal structures and phase contents of HPH-prepared 2D hBN flakes and bulk hBN were investigated using X-ray diffraction (XRD) and Raman spectroscopy. Fig. 1a compares the XRD patterns of HPH-processed 2D hBN flakes and bulk hBN. During HPH exfoliation, no impurities were observed, as shown in the XRD patterns of the HPH-processed 2D hBN flakes and bulk hBN. The XRD patterns of the HPH-prepared 2D hBN flakes can be indexed to the diffraction peaks corresponding to (002), (100), (101), (102), (004), (103), (104), and (110) lattice planes, respectively.[36] The XRD patterns exhibit distinct broad diffraction peaks, which indicate the preparation of a crystalline 2D hBN structure using the HPH method. The exfoliation of bulk hBN was confirmed by the increased intensity of the (002) planes in the HPH-prepared 2D hBN flakes, suggesting that the exfoliation took place along this plane without destroying the crystalline structure. Moreover, a shift in the (002) planes was observed for the HPH-prepared 2D hBN flakes compared with bulk hBN (Fig. 1b). The crystalline structure of the 2D hBN flakes remained intact after exfoliation with HPH. The results show that the structural integrity of 2D hBN flakes is not compromised and retains its original properties, enabling high-quality exfoliated hBN. Fig. 1c and d compare the Raman

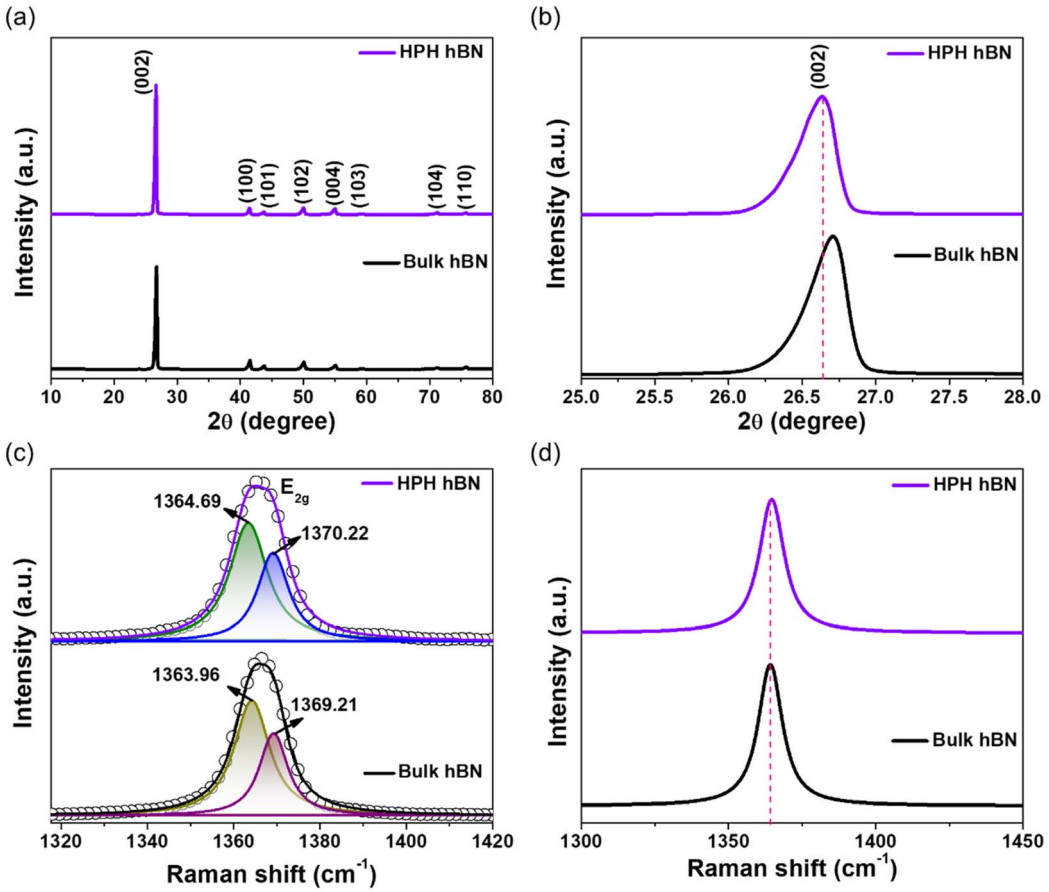

Fig. 1 (a and b) XRD patterns and (c and d) Raman spectra of HPH processed 2D hBN flakes and bulk hBN.

spectra of the HPH-prepared 2D hBN flakes and bulk hBN. The characteristic intense peak corresponding to the E_{2g} vibration mode of hBN was observed for the HPH-prepared 2D hBN flakes and bulk hBN.[36] The full-width at half-maximum (FWHM) in E_{2g} mode was approximately 6.5 cm^{-1} for HPH-prepared 2D hBN flakes. This value is greater than the FWHM of boron nitride (BN) powder previously reported (4.77 cm^{-1}).[37] The E_{2g} mode of HPH-prepared 2D hBN flakes exhibits a slight blue shift compared to bulk hBN due to interlayer interactions that elongate B–N bonds in the bulk material. These observations indicate the exceptional quality of the 2D hBN flakes, suggesting that HPH is an effective and scalable route for exfoliating bulk materials.

The morphologies of the HPH-prepared 2D hBN flakes were investigated using scanning electron microscopy (SEM). Fig. 2a and b shows randomly dispersed thin 2D hBN flakes. The size of 2D hBN flakes ranges from hundreds of nanometers to several micrometers. The statistical distribution of the lateral sizes of the HPH-prepared 2D hBN flakes was estimated by SEM analysis. Fig. S1a† shows a representative SEM image of the HPH-prepared 2D hBN flakes, and a histogram illustrates the distribution of lateral sizes of the flakes (Fig. S1b†). The histogram clearly shows the variation from nanometers to micrometers. Fig. S2† shows the dielectric properties of hBN. The dielectric properties of the material were measured using a configuration consisting of a ~3.5 μm thick film (Fig. S3†) with an area of 1 cm^2 and Al electrodes placed on both the top and bottom of the film. Capacitance was measured using an impedance analyzer (4200A SCS) after applying a 3 V signal across a frequency range of 8–4 MHz. The dielectric constant (k) was calculated using eqn (1).

$$k = \frac{Cd}{\varepsilon_0 A} \quad (1)$$

where C is the measured capacitance of the material, d is the thickness of the material layer, A is the area of the electrodes, and ε_0 is the permittivity of free space (8.854×10^{-12} F m^{-1}).

Furthermore, the transmission electron microscope (TEM) was used to examine the surface morphology of the HPH-prepared 2D hBN flakes. Fig. 2c shows TEM images of several stacked layers of 2D hBN flakes with diameters of several nanometers. Further, the statistical distribution of the lateral sizes of the 2D hBN flakes was investigated from the TEM images (Fig. S1c and d†). Similar to the SEM analysis, the histogram shows the variation in the hBN size obtained using the HPH method. The SEM and TEM images show thin, layered structures with varying lateral sizes, and statistical analysis reveals a clear peak in size distribution, indicating controlled exfoliation. The differences between the SEM and TEM analyses suggest that TEM provides a more precise measurement of

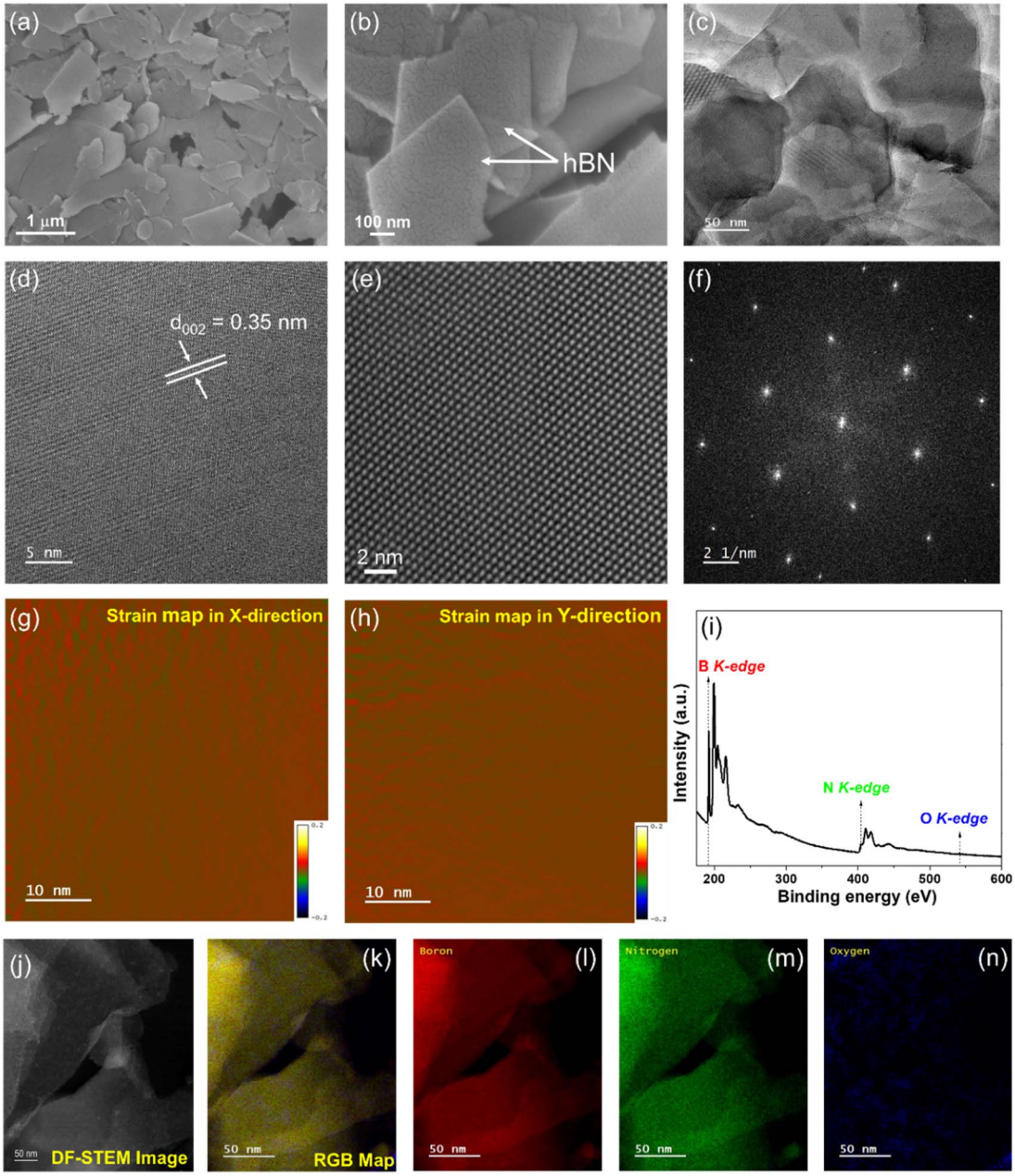

Fig. 2 (a and b) SEM images, (c) TEM image, (d) HRTEM image, (e) atomic-scale HRTEM image, (f) corresponding FFT, (g) strain map in *X*-direction, (h) strain map in *Y*-direction, (i) core-loss EELS spectra, (j) STEM-HADDF image, and (k–n) EELS elemental mapping of the HPH-prepared 2D hBN flakes.

smaller flakes because of their higher resolution. These results demonstrate HPH's efficiency in producing uniform 2D hBN flakes for energy harvesting and advanced electronic applications. The high-resolution TEM (HRTEM) image of 2D hBN flakes with an interplanar spacing of 0.35 nm corresponds to the (002) plane of hBN, as shown in Fig. 2d.[38] The typical atomic structure of 2D hBN flakes is shown in Fig. 2e. The corresponding Fast Fourier Transform (FFT) revealed hexagonal symmetry in the lattice of the 2D hBN flakes, demonstrating the crystalline nature of the HPH-prepared 2D hBN flakes (Fig. 2f). Thus, these shows that HPH technique is beneficial for producing ultra-thin 2D flakes or nanosheets with over 90% yield.

The strain maps in the *X* and *Y* directions for the HPH-prepared 2D hBN flakes are shown in Fig. 2g and h, illustrating the strain variation along the horizontal *X*-direction. The red (positive value) regions indicate expansion, while the blue (negative value) regions indicate compression along the *X*-direction, respectively (Fig. 2g). Defects in hBN, such as vacancies, dislocations, grain boundaries, and adsorbates, influence strain differently depending on their orientation. Differences in the strain distribution significantly affected the mechanical

properties. The HPH-synthesized hBN flakes are free of planar defects and dislocations (line defects), as illustrated in the strain maps in the *X*- and *Y*-directions (Fig. 2g and h).

The electron energy loss spectroscopy (EELS) spectrum of the HPH-processed 2D hBN flakes is shown in Fig. 2i. The red and green lines represent the boron (B) and nitrogen (N) K-

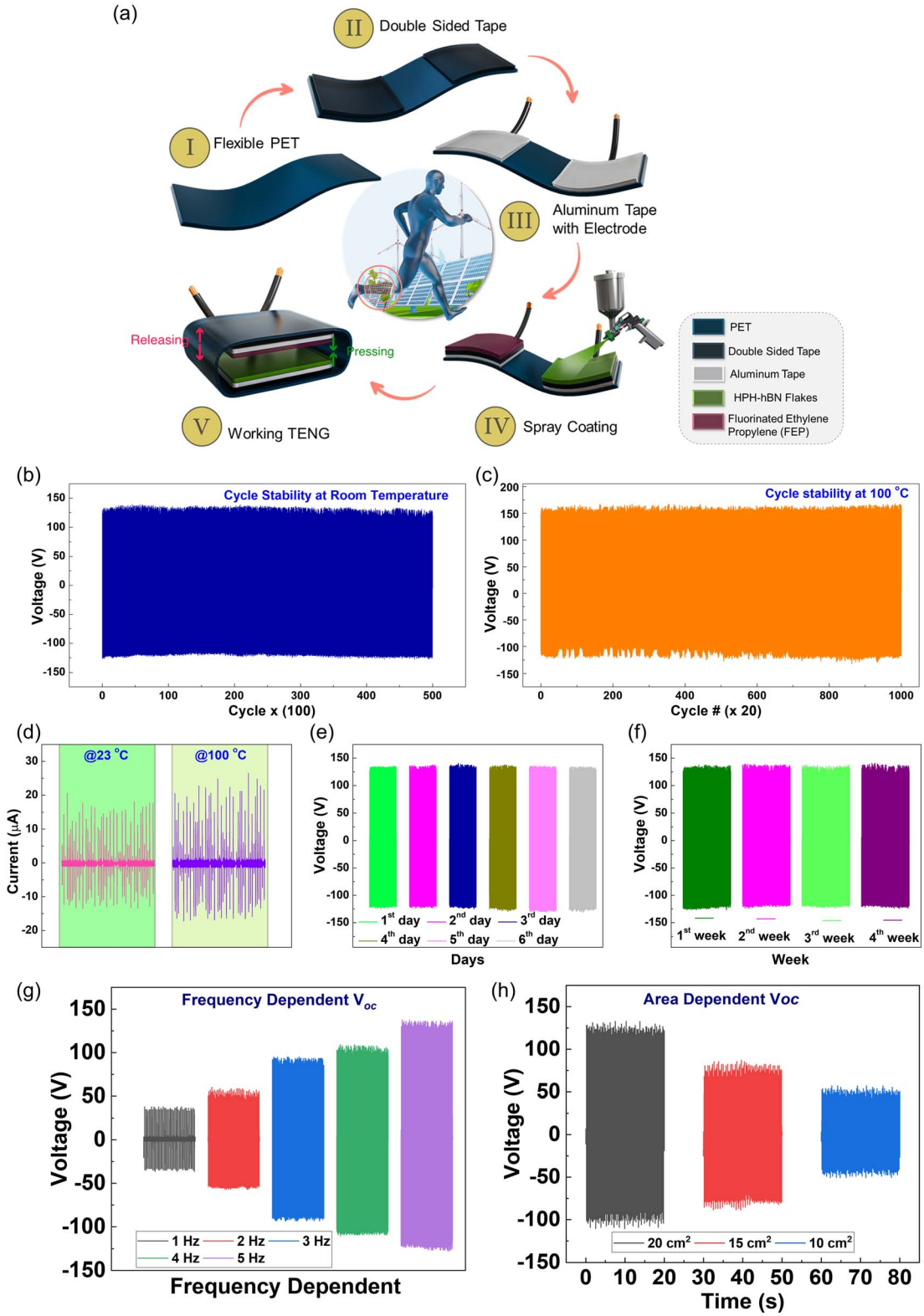

Fig. 3 (a) Schematics of the fabrication and output characteristics of the HPH-prepared 2D hBN flake-based TENG, (b) continuous cycle at room temperature, (c) continuous cycles at 100 °C, (d) short circuit current at room temperature and 100 °C, (e) voltage generation for six consecutive days, (f) V_{oc} for one month, (g) voltage at different tapping frequencies, and (h) voltage at different device size.

edges. The acquired EELS spectrum provides evidence of the formation of hBN flakes. The high annular darkfield scanning transmission microscope (STEM-HADDF) image confirms the presence of 2D hBN flakes, as shown in Fig. 2j. Fig. 2k–n shows the EELS elemental mapping of the HPH-prepared 2D hBN flakes. The EELS elemental mapping indicates a uniform presence of B and N corresponding to the hBN flakes, as shown in Fig. 2l and m. The presence of oxygen (O) may have resulted from the surrounding environmental conditions (Fig. 2n).

Fabrication and output characteristics of TENG

Fig. 3a shows the contact-separation (CS) mode of the HPH-prepared 2D hBN flake-based TENG and its electrical output characteristics. Fig. 3a(I) shows the CS-mode hBN-based TENG configuration, in which a thick flexible poly(ethylene terephthalate) (PET) substrate of 12 cm × 5 cm was used as the base material for the fabrication (Fig. 3a(I)), followed by the attachment of thin double-sided tapes of size 4 cm × 5 cm separated by nearly 2 cm, as depicted in Fig. 3a(II). Herein, the PET substrate acted as a supporting structure for the stability of the overall device. It provides necessary separation and helps the recoil/separation of electronegative and electropositive materials when the force or compressed force is released. Then, two aluminum (Al) foils of size 4 cm × 5 cm connected with a copper wire are attached with these double-sided tapes with high-tack adhesive side on the upward side to attach electropositive and electronegative spray-coated on the second Al foil, as shown in Fig. 3a(III). Finally, a 4 cm × 5 cm FEP thin layer was connected to the sticky side of the Al foil, and hBN was spray-coated on the opposite Al foil as shown in Fig. 3a(IV), and dried in an ambient environment at 60 °C for 2 h. Finally, the base PET substrate was folded with a small gap between the FEP and hBN layer for tapping to extract the open circuit voltage (V_{oc}) and short circuit current (I_{sc}), as shown in Fig. 3a(V). The damping force of 10 N was measured using a DY220 load cell controller equipped with a digital display meter and a DYHW-116 mini button load cell with a 10 kg compression force sensor. The output characteristics, $V_{oc,}$ and I_{sc} of hBN-TENG were analyzed at room temperature and 100 °C. Fig. 3b and c shows the V_{oc} of the TENG as 132 V and 150 V at room temperature and 100 °C, respectively, for more than 50 000 cycles. The I_{sc} values for the hBN-TENG were calculated as 19 μA and 28 μA at room temperature and 100 °C, as depicted in Fig. 3d. To confirm the stability of the TENG with time, the V_{oc} was analyzed on seven consecutive days and later for one month, as shown in Fig. 3d and e. These characteristics imply that hBN-TENG can harvest energy for portable devices and devices for the Internet of Things (IoT) for a long time. The V_{oc} values of hBN-TENG are investigated with the different tapping frequencies (Fig. 3g) and effective contact areas (Fig. 3h) of the electropositive and electronegative materials. V_{oc} increased with tapping frequency and contact area. To ensure that the device's output is solely due to the triboelectric effects, we prepared a piezoelectric nanogenerator with an Al/hBN/Al configuration designed to isolate the piezoelectric effect. The open-circuit voltage and short-circuit current for the piezoelectric nanogenerator were measured, yielding values of 4 V and 200 nA, respectively, as shown in Fig.s S4a and b.† These measurements confirm that the piezoelectric effect in the hBN layer generates an output that is separate from the triboelectric effect. In our experiments, we carefully ensured that the triboelectric nanogenerator (TENG) used in the main study did not exhibit any significant piezoelectric contribution. The device was characterized under conditions in which only triboelectrification caused by repeated contact and separation between the hBN and FEP layers was active. As the piezoelectric output from the hBN was measured separately and found to be significantly lower than the triboelectric output from the TENG, we can confidently conclude that the device's performance in the main study is primarily attributed to the triboelectric effect. This experimental approach, including the isolation of the piezoelectric and triboelectric contributions, ensures that the observed output is predominantly from triboelectrification, confirming the absence of substantial piezoelectric interference in the device's operation.

Furthermore, to systematically demonstrate the advantages of the HPH method for developing hBN, we compared the performance of TENG devices fabricated using bulk hBN (Fig. S5a†) and commercially available hBN (Fig. S5b†) as triboelectric layers. Our results indicate that the bulk hBN-based TENG generates a V_{oc} of ∼67 V. In contrast, the commercial hBN-based TENG produces a V_{oc} of ∼98 V. Notably, the TENG device utilizing HPH-derived hBN flakes (V_{oc} of ∼135 V) exhibits superior performance, clearly highlighting that HPH is a scalable and efficient method for achieving enhanced triboelectric performance.

Mechanism of output characteristics

Fig. 4 shows the polarity/phase-dependent V_{oc} of hBN-TENG and its mechanism. Fig. 4a and b depicts the phase-dependent V_{oc} and I_{sc} values of the hBN-TENG, respectively, illustrating that the voltage and current generated are purely from the triboelectric effect of the hBN flake-based TENG and not from any noise. The V_{oc} peaks for the positive and negative polarities were calculated as 134 V and −120 V, respectively. The peak voltage at negative polarity implies that hBN-TENG efficiently converts mechanical energy into electrical energy. The connection of a full wave rectifier with an out-of-TENG converts effective signals into output signals. Fig. 4c shows the magnified output of one complete cycle of the TENG, which demonstrates the clean output of V_{oc}. Unlike most TENGs,[17–19] the V_{oc} values for both positive and negative phases were nearly equal in magnitude, so I_{sc}. This leads to several benefits of TENG, including enhanced output power compared to when there is a significant V_{oc} imbalance, reliable performance with time, reduced electrical noise, which is helpful when a precise signal is needed, and overall improved energy conversion efficiency. A clean V_{oc} signal for one complete cycle (Fig. 4c) further demonstrates that hBN plays a vital role in obtaining stable and enhanced device efficiency.

The working mechanism of the vertical CS hBN-TENG is illustrated schematically in Fig. 4d. Both layers were in a charge-

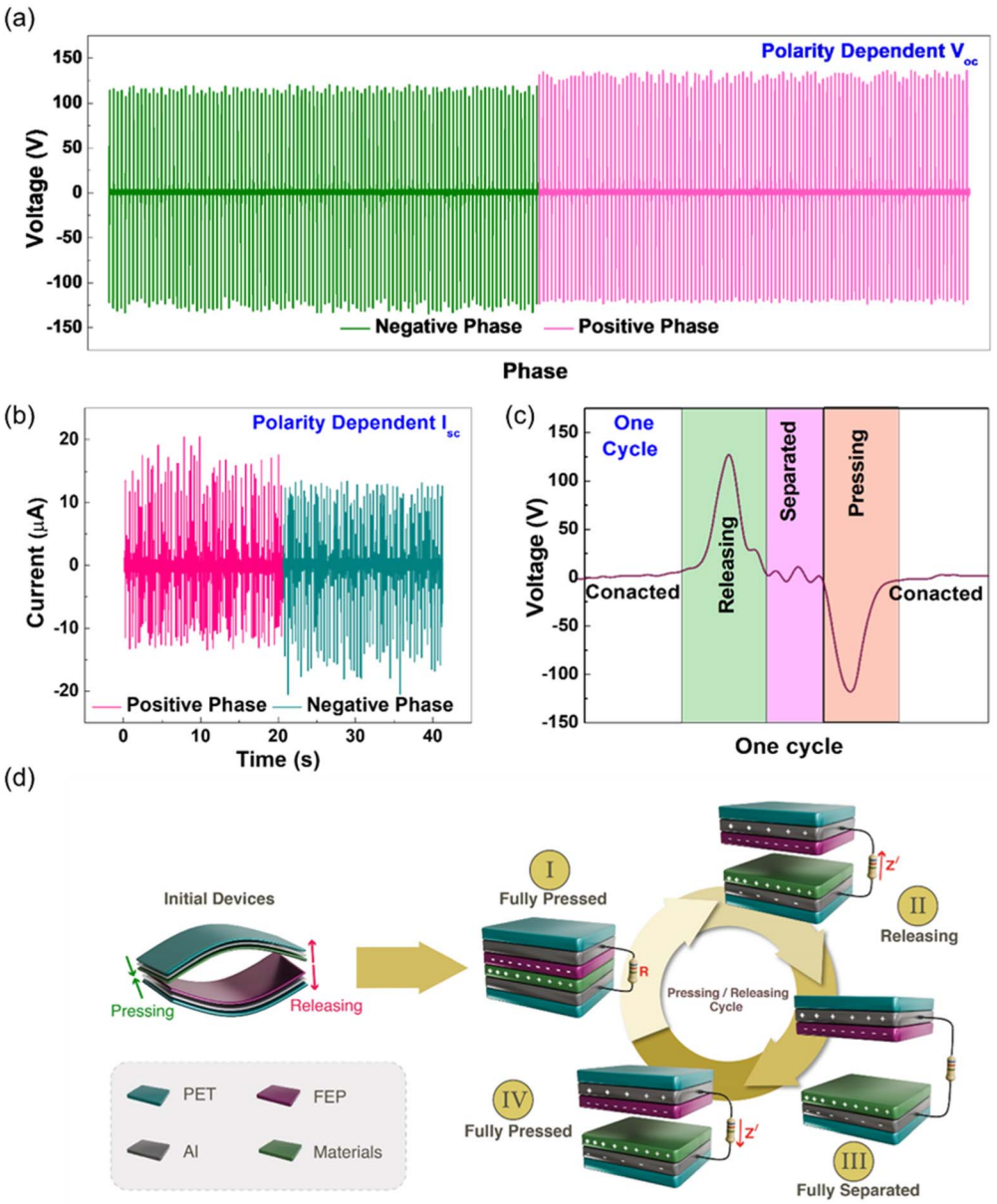

Fig. 4 Polarity dependent (a) open circuit voltage, (b) short circuit current, (c) one complete cycle showing the smooth output signal, and (d) mechanism of output characteristics.

balanced state in the initial state because the hBN and FEP layers were separated. Fig. 4d(I) pressed state: when both layers are in contact with the external force, hBN is positively charged, and FEP is negatively charged because hBN is electropositive, and FEP is an electronegative material. Due to charge transfer, the faces of the triboelectric layers receive opposite charges; *i.e.*, hBN will be positive, and PET will be negative. Fig. 4d(II) release: during release, charge is induced in the Al tapes, and electrons flow from the top to the bottom layer of the hBN-TENG. Fig. 4d(III) fully released: when hBN-TENG reaches a fully released state, the charge will reach equilibrium, and no more electric fields will change between the layers; hence, V_{oc} and I_{sc} will be zero. Fig. 4d(IV) compression: during compression, the charge/electrons start to flow in opposite directions or reversibly compared to the releasing state of the TENG, as schematically shown, between the triboelectric layers come in contact. Hence, the alternating and FEP layers of the TENG were used.

To provide further insight into the device's triboelectric behavior, the electrostatic surface potentials of the tribo-layers were measured. The electrostatic surface potentials of the tribo-layers were measured using a KEYENCE handheld electrostatic sensor (SK-050) in non-contact mode. These measurements were taken immediately after 50 contact-separation cycles between the positive (hBN) and negative (FEP) layers with a 10 N load and a frequency of 5 Hz. The enhancement of

electrostatic charge in the TENG was due to the continuous contact and separation between the dielectric layers, which amplified the triboelectric effect. Without tapping, the electrostatic charges on the hBN and FEP films were measured, revealing limited electron transfer and low charge accumulation. However, when tapping was introduced, a substantial increase in charge density was observed, creating a stronger electrostatic field that directly improved the TENG's performance by generating more electrical energy, as illustrated in Fig. S6a and b.† Electrostatic charge measurements on the electropositive hBN film and the electronegative FEP film before and after tapping demonstrated a significant increase in charge accumulation due to triboelectrification. Specifically, the charge on the hBN film increased from 120 to 510 V, while the FEP film's charge increased from −210 to −750 V after tapping, as shown in Fig. S6a and b.† These results indicate that the tapping process significantly enhances the triboelectric properties of the device, leading to improved charge transfer and higher energy generation. The substantial increase in the electrostatic charge on both films further confirms the successful optimization of the device structure, resulting in more efficient energy harvesting and improved TENG performance.

Using an electron cloud interaction model, Fig. S7† illustrates the contact electrification process between the hBN and FEP layers. In this model, d represents the distance between the electron clouds of the two materials, and E1 and E2 correspond to the potential energy required for electrons to escape their respective orbits. Ep and En denote the electron energy levels within the hBN and FEP atomic structures, respectively. Initially, when the hBN and FEP layers are separated, their electron clouds do not overlap, meaning that the electrons are tightly bound to their original orbitals. In this state, a high-energy barrier prevents electron transfer between the materials. However, when mechanical forces are applied and the hBN and FEP layers come into direct contact, the electron clouds of the two materials begin to overlap. This overlap reduces the interatomic potential barrier, facilitating electron escape from their original orbits. As a result, high-energy electrons from the tribopositive hBN layer transfer to tribonegative FEP layer, continuing this transfer until equilibrium is reached. The overlap of the electron clouds forms an asymmetric double-well potential upon contact, which facilitates the movement of electrons between the two materials. Once the layers are separated again, the transferred electrons remain trapped within the hBN layer because of the re-established energy barrier, which prevents the electrons from returning to the FEP layer. This trapping effect ensures that the charge difference between the two materials is maintained unless external conditions (such as mechanical force or environmental factors) change, thereby sustaining the charge separation between the hBN and FEP layers.

hBN-TENG as a self-powered device

Environmental changes such as humidity, temperature, and even pressure can influence the output characteristics of a TENG. To monitor these environmental changes, the hBN-TENG was maintained under different humidity and temperature conditions. The V_{oc} of the TENG is shown in Fig. 5. The monitoring of different relative humidity (% RH) was carried out by keeping the TENG in a closed chamber with the standard humidity sensor to calculate the point at which the tapping could be carried out, as shown in Fig. 5a. Fig. 5b demonstrates TENG's response to the temperature increase. When the temperature is increased from room temperature 25 °C to 100 °C in steps of 20 °C, a gradual increase in V_{oc} is observed. The increase in V_{oc} and I_{sc} with increasing temperature is due to the cumulative effect of reduced dielectric constant, improved triboelectric charge generation, enhanced charge density at triboelectric surfaces, and activation of trapped charges in the triboelectric layers, particularly in hBN. Hence, these effects lead to more charge transfer, and improve V_{oc} and I_{sc} at elevated temperatures. Fig. S8† shows the dependence of V_{oc} on temperatures ranging from 20 °C to 300 °C. V_{oc} increased with increasing temperature up to 140 °C, and decreased until reaching 105 V at 300 °C. The increase in V_{oc} with increasing temperature is due to the cumulative effect of the reduced dielectric constant, improved triboelectric charge generation, enhanced charge density at triboelectric surfaces, and activation of trapped charges in the triboelectric layers, particularly in hBN. However, the V_{oc} decreased at temperatures higher than 140 °C and reached lower than the V_{oc} at 20 °C, particularly due to structural deformation, interface degradation, and chemical changes in the electronegative electrodes, *i.e.*, FEP. The % RH of the chamber was varied by humidification and dehumidification, and V_{oc} was measured simultaneously. The humidity in the closed chamber increased from lab humidity (30% RH) to 100% RH in steps of 10%, as shown in Fig. 5c, and the observed V_{oc} decreased linearly with the increase in humidity. For the % RH values of 30, 40, 50, 60, 70, 80, 90, and 100, the calculated V_{oc} values were 132, 118, 108, 93, 66, 53, 33, and 11 V, respectively.

After achieving 100% RH, the closed chamber was opened to reduce humidity, and finally, 30% RH was achieved at the TENG ambient. With the decrease in humidity, water desorption also occurred in the hBN layer, which consequently increased the V_{oc} of hBN-TENG, as shown in Fig. 5d. As the % RH decreased from 100% to 30% in step 10, the V_{oc} was calculated as 12, 39, 50, 72, 80, 103, 119, and 132 V, respectively. The combined effect of reduced electronegativity of hBN, reduced charge transfer in the compressed state of TENG, and an increase in dielectric constant between triboelectric layers, *i.e.*, electronegative and electropositive layers, results in a decrease in V_{oc} with an increase in humidity. This suggests that hBN-TENG is a full-range self-powered humidity sensor with excellent repeatability. The open circuit voltages were generated using physiological motions by hand and foot on the TENG, and V_{oc} was monitored for different mechanical (soft and hard-hitting) inputs, as shown in Fig. 5e and f. The hBN-TENG generated different peak V_{oc} values for walking and running (Fig. 5e). While walking, the device experiences a slight force/pressure; while running, the device experiences a higher force/pressure. Therefore, walking generates V_{oc} of 200 V, and running generates a peak voltage of 300 V. The energy harvesting capability of

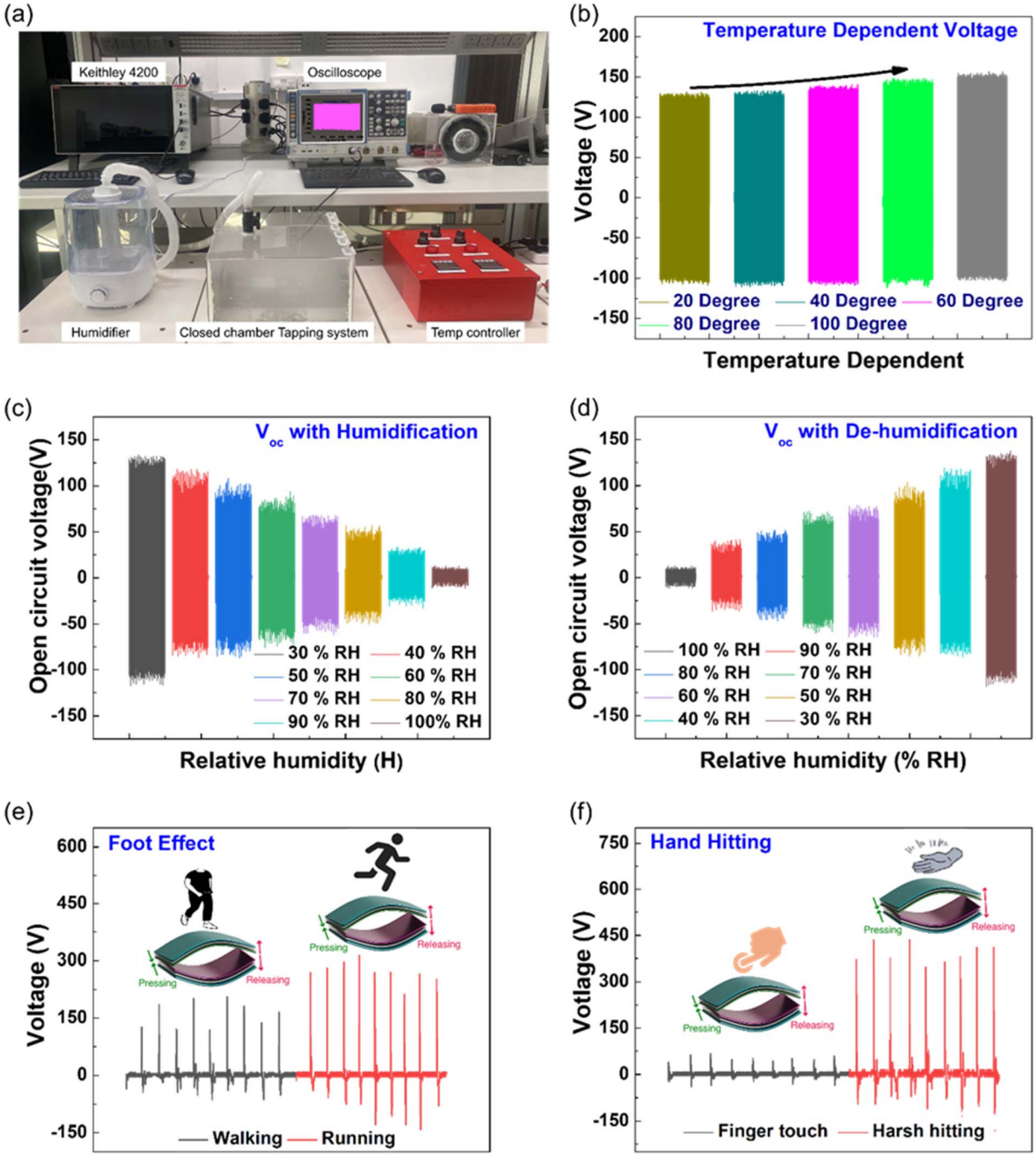

Fig. 5 Self-powered monitoring of environment changes using devices showing (a) humidity measurement step up, (b and c) capability of the device to monitor environment humidity range from 20% RH to 100% RH for humidification and de-humidification (d) response of TENG on different temperatures and (e and f) sensitivity for TENG for different tapping pressures.

the device was further investigated by soft tapping with one finger and harsh hitting with the full hand, as shown in Fig. 5f. Soft tapping generated a peak voltage of 50 V, and harsh tapping gave a peak V_{oc} of 450 V. This demonstrates that hBN-TENG can sense different input pressures with unique V_{oc} values. V_{oc} values can be expressed as follows: to measure the input pressure on the device.

hBN-TENG for energy harvesting and powering portable devices

TENG produces V_{oc} signals during pressing and releasing, limiting their direct use for small power-consuming electrical appliances that require a constant/consistent power supply. This makes TENG less competitive in the power source market. Therefore, a circuit was developed using a rectifier and a connected capacitor to store input mechanical energy in charge or

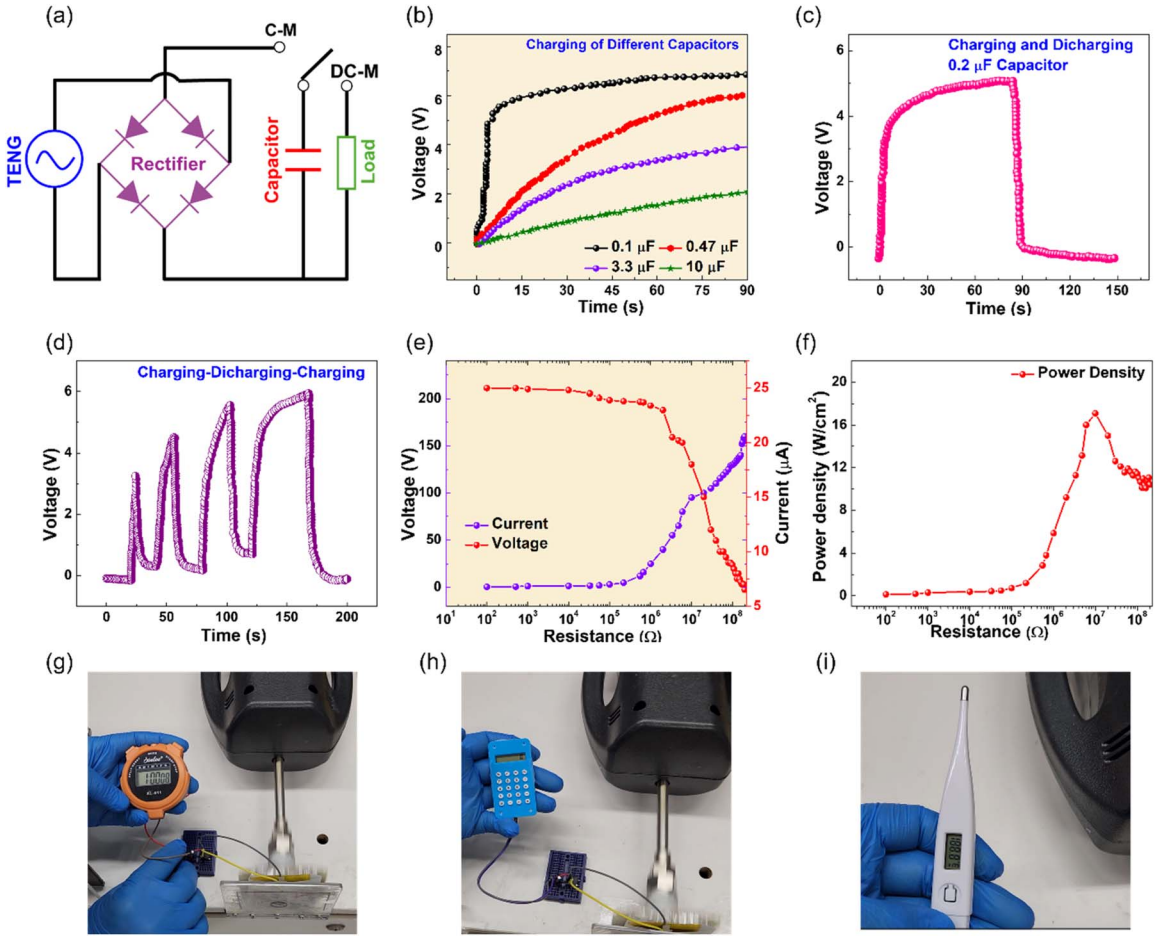

Fig. 6 Demonstration of energy conversion and powering portable devices showing (a) circuit diagram for the energy storage, (b) charging of different capacitors, (c and d) charging and discharging of 2 μF capacitor for continuous energy harvesting, (e) voltage and current across the different resistors and (f) power density corresponding to the different resistors, and (g–i) the powering of portable devices.

electrical energy. Fig. 6 shows the capacity of the hBN-TENG to store energy in the form of charge/electric energy, operate commercial portable low-power appliances, and consume power across known resistors. Fig. 6a shows the circuit diagram consisting of a TENG, a capacitor, a bridge rectifier, a load, and switches for storing mechanical energy in the form of electrical energy in the capacitor and consumption across the load. The load could be an IoT device that can be operated with the help of an open stored switch, and for discharge, the switch between the load and the capacitor is closed. The capability of hBN-TENG is demonstrated by connecting different capacitors with capacitances 0.1, 0.47, 3.3, and 10 μF and measuring the voltage across each capacitor (Fig. 6b). A demonstration of operating these portable devices is provided in ESI Movies 1–3.† The charging and discharging of the capacitor of capacitance 0.2 μF are monitored in an oscilloscope with an internal resistance of 120 MΩ and the time evolution of the voltage across the capacitor during the charging and discharging process, as shown in Fig. 6c and d. The continuous charging and discharging of the capacitor with continuous mechanical input (pressing/releasing by tapping) in hBN-TENG indicate that this device can harvest energy from mechanical input in an energy-efficient lift style (Fig. 6e and f). After charging the capacitor of 0.47 μF for about 90 s, the stored energy was successfully used to turn on/operate the commercially available portable stopwatch, mini-calculator, and thermometer, as shown in Fig. 6g–i and Videos S1–S3.† The TENG performances of the HPH-synthesized hBN flakes and other synthesis methods of hBN-based state-of-the-art TENGs are compared in Table S1.† The comparison illustrates that the I_{sc} and P_d values of our HPH-hBN-based TENG in this work outperformed most hBN-based state-of-the-art TENGs. The P_d values of our HPH-hBN-based TENG are probably the highest reported thus far for an hBN-based TENG. As a result, we expect that the scalable production of hBN by the HPH method will facilitate the development of 2D functional materials for high-performance energy harvesting and storage applications.

Conclusion

In summary, we synthesized highly pure 2D hBN flakes using the HPH method. The SEM and HRTEM images show flake sizes of ~2.5 μm. In a 4 cm × 5 cm contact-separation mode, the TENG, hBN, and FEP layers were used as the electropositive and

electronegative triboelectric layers. The HPH-hBN-based -TENG device demonstrated long-term repeatable mechanical energy harvesting at room temperature and 100 °C. The fabricated TENG generated an open circuit voltage peak of 135 V and short circuit current of 17 μA with a power density of 18 W cm^{-2}. The peak voltages of the positive and negative phases were 134 and 123 V, respectively, which ensured the high-power supply of the designed TENG. In addition, the device could respond distinguishably to the full range of humidity (30–100% RH) and applied pressure. The continuous charging and discharging of a 0.2 μF capacitor and powering of portable devices such as stopwatches, digital thermometers, and mini calculators imply that the designed TENG can be an excellent candidate for the continuous harvesting of mechanical energy to electrical energy to operate IoT and portable devices.

Data availability

The data supporting the findings of this article are included in the ESI.†

Author contributions

Yawar Abbas and Rohan B. Ambade contributed equally to this work. Conceptualization: Y. A., R. B. A., M. U. K., and Y. A. S.; methodology: Y. A., R. B. A., M. U. K., and Y. A. S.; investigation: Y. A., R. B. A., M. U. K., R. C., Y. Z., B. M., D. A., and Y. A. S.; writing – review & editing, Y. A., R. B. A.; M. U. K., and Y. A. S.; supervision and funding acquisition, Y. A. S.; all authors contributed to reading and commenting on the manuscript.

Conflicts of interest

There are no conflicts of interest to declare.

Acknowledgements

This research was supported by funding from the Research & Innovation Center for Graphene and 2D Materials (RIC-2D), FSU project code 8474000463, System on Chip Lab grant under Awards No. 8474000134 and 8474000137, Advanced Research and Innovation Center (ARIC), jointly funded by STRATA Manufacturing PJSC (a Mubadala company), and Sandooq Al Watan under Grant SWARD-S22-015, from the Khalifa University of Science and Technology. The authors thank the Imaging and Characterization (IAC) core lab facility of King Abdullah University of Science & Technology (KAUST) for granting access to its transmission electron microscopes lab to carry out the TEM analysis of the samples.

References

1 X. Li, G. Xu, X. Xia, J. Fu, L. Huang and Y. Zi, *Nano Energy*, 2019, **56**, 40–55.
2 A. Ahmed, I. Hassan, M. F. El-Kady, A. Radhi, C. K. Jeong, P. R. Zu, J. Selvaganapathy, S. Ren, Q. Wang and R. B. Kaner, *Adv. Sci.*, 2019, **6**, 1802230.
3 K. Xia, D. Wu, J. Fu, N. A. Hoque, Y. Ye and Z. Xu, *J. Mater. Chem. A*, 2020, **8**, 25995–26003.
4 W. G. Kim, D. W. Kim, I. W. Tcho, J. K. Kim, M. S. Kim and Y. K. Choi, *ACS Nano*, 2021, **15**, 258–287.
5 S. Wang, L. Lin, Y. Xie, Q. Jing, S. Niu and Z. L. Wang, *Nano Lett.*, 2013, **13**, 2226–2233.
6 S. Anwer, M. U. Khan, M. B. Rezeq, M. D. Cantwell, W. D. Gan and L. Zheng, *J. Chem. Eng.*, 2023, **470**, 144281.
7 X. Yin, D. Liu, L. Zhou, X. Li, C. Zhang, P. Cheng, H. Guo, W. Song, J. Wang and Z. L. Wang, *ACS Nano*, 2018, **13**, 698–705.
8 W. He, W. Liu, J. Chen, Z. Wang, Y. Liu, X. Pu, H. Yang, Q. Tang, H. Yang, H. Guo and C. Hu, *Nat. Commun.*, 2020, **11**, 4277.
9 J. Wang, W. Ding, L. Pan, C. Wu, H. Yu, L. Yang, R. Liao and Z. L. Wang, *ACS Nano*, 2018, **12**, 3954–3963.
10 W. Sun, Z. Jiang, X. Xu, Q. Han and F. Chu, *Int. J. Mech. Sci.*, 2021, **207**, 106668.
11 D. Ren, H. Yang, X. Zhang, Q. Li, Q. Yang, X. Li, P. Ji, P. Yu, Y. Xi and Z. L. Wang, *Adv. Energy Mater.*, 2023, **13**, 2302877.
12 W. Akram, Q. Chen, G. Xia and J. Fang, *Nano Energy*, 2023, **106**, 108043.
13 Y. Yang, H. Zhang, J. Chen, Q. Jing, Y. S. Zhou, X. Wen and Z. L. Wang, *ACS Nano*, 2013, **7**, 7342–7351.
14 Y. Wang, J. Duan, X. Yang, L. Liu, L. Zhao and Q. Tang, *Nano Energy*, 2020, **69**, 104418.
15 I. Kim, H. Jeon, D. Kim, J. You and D. Kim, *Nano Energy*, 2018, **53**, 975–981.
16 D. Lei, J. Wu, Y. Zi, C. Pan, H. Cui and X. Li, *ACS Appl. Electron. Mater.*, 2023, **5**, 2819–2828.
17 B. G. Hyun, Y. S. Jun, J. H. Lee, M. Hamidinejad, Z. Saadatnia, S. Ghaffari-Mosanenzadeh, H. E. Naguib and C. B. Park, *Composites, Part B*, 2024, **272**, 111193.
18 A. S. Bhavya, H. Varghese, A. Chandran and K. P. Surendran, *Nano Energy*, 2021, **90**, 106628.
19 A. S. Bhavya, H. Varghese, A. Chandran and K. P. Surendran, *ACS Appl. Electron. Mater.*, 2023, **5**, 5483–5493.
20 A. Geim and K. Novoselov, *Nat. Mater.*, 2007, **6**, 183–191.
21 R. B. Ambade, K. H. Lee, D. J. Kang and T. H. Han, *Acc. Mater. Res.*, 2023, **4**, 389–402.
22 W. Eom, H. Shin, R. B. Ambade, S. H. Lee, K. H. Lee, D. J. Kang and T. H. Han, *Nat. Commun.*, 2020, **11**, 2825.
23 Y. A. Samad, Y. Li, A. Schiffer, S. M. Alhassan and K. Liao, *Small*, 2015, **11**, 2380–2385.
24 Y. A. Samad, Y. Li, S. M. Alhassan and K. Liao, *ACS Appl. Mater. Interfaces*, 2015, **7**, 9195–9202.
25 S. B. Ambade, R. B. Ambade, W. Eom, S. H. Noh, S. H. Kim and T. H. Han, *Adv. Mater. Interfaces*, 2018, **5**, 1801361.
26 K. S. Novoselov, A. Mishchenko, A. Carvalho and A. H. C. Neto, *Science*, 2016, **353**, 6298.
27 J. D. Caldwell, I. Aharonovich, G. Cassabois, J. H. Edgar, B. Gil and D. N. Basov, *Nat. Rev. Mater.*, 2019, **4**, 552–567.
28 S. Mitra, Á. Jiménez-Galán, M. Aulich, M. Neuhaus, R. E. F. Silva, V. Pervak, M. F. Kling and S. Biswas, *Nature*, 2024, **628**, 752–757.
29 A. Pakdel, Y. Bando and D. Golberg, *Chem. Soc. Rev.*, 2014, **43**, 934.

30 K. K. Kim, H. S. Lee and Y. H. Lee, *Chem. Soc. Rev.*, 2018, **47**, 6342–6369.
31 P. G. Karagiannidis, S. A. Hodge, L. Lombardi, F. Tomarchio, N. Decorde, S. Milana, I. Goykhman, Y. Su, S. V. Mesite, D. N. Johnstone, R. K. Leary, P. A. Midgley, N. M. Pugno, F. Torrisi and A. C. Ferrari, *ACS Nano*, 2017, **11**, 2742–2755.
32 J. Shang, F. Xue, C. Fan and E. Ding, *Mater. Lett.*, 2016, **181**, 144–147.
33 Y. Chen, Y. Liu, X. Liu, P. Li, Z. Li, P. Jiang and X. Huang, *Small Methods*, 2024, 2301386.
34 T. J. Nacken, C. Damm, J. Walter, A. Rüger and W. Peukert, *RSC Adv.*, 2015, **5**, 57328–57338.
35 X. Qi, H.-B. Zhang, J. Xu, X. Wu, D. Yang, J. Qu and Z.-Z. Yu, *ACS Appl. Mater. Interfaces*, 2017, **9**, 11025–11034.
36 V. Guerra, C. Wan, V. Degirmenci, J. Sloan, D. Presvytis and T. McNally, *Nanoscale*, 2018, **10**, 19469–19477.
37 M. Du, Y. Wu and X. Hao, *CrystEngComm*, 2013, **15**, 1782–1786.
38 N. Mittal, G. Kedawat, Kanika, S. Gupta and B. K. Gupta, *ChemistrySelect*, 2020, **5**, 12564–12569.